

A Finite-Difference Time-Domain approach for dispersive magnetic media

JASMIN GRAF,^{1,2,3,4*} JOSHUA BAXTER,^{4,5} SANCHAR SHARMA,^{1,2}
SILVIA VIOLA KUSMINSKIY,^{1,2,4} LORA RAMUNNO,^{4,5,6}

¹*Institut für Theoretische Festkörperphysik, RWTH Aachen University, 52056 Aachen, Germany*

²*Max Planck Institute for the Science of Light, 91058 Erlangen, Germany*

³*Friedrich-Alexander-Universität Erlangen-Nürnberg, Department of Physics, 91058 Erlangen, Germany*

⁴*Max Planck-uOttawa Centre for Extreme and Quantum Photonics, University of Ottawa, ON, K1N 6N5 Ottawa, Canada*

⁵*Department of Physics, University of Ottawa, ON, K1N 6N5 Ottawa, Canada*

⁶*Nexus for Quantum Technologies Institute, University of Ottawa, ON, K1N 6N5 Ottawa, Canada*

*jasmin.graf@mpl.mpg.de

Abstract: We extend the Finite-Difference Time-Domain method to treat dispersive magnetic media by incorporating magneto-optical effects through a frequency-dependent permittivity tensor. For benchmarking our method, we consider the light scattering on a magnetic sphere in the Mie regime. We first derive the analytical scattering expressions which predict a peak broadening in the scattering efficiency due to the atomic energy level splitting in the presence of a magnetic field, together with an additional rotated part in the scattered field profile due to the Faraday rotation. We show that our numerical method is able to capture the main scattering features and discuss its limitations and possible improvements in accuracy.

1. Introduction

Magneto-optical (MO) materials, in which the magnetization affects the polarization of optical photons, are vital for non-reciprocal optical technologies such as circulators and isolators [1]. Garnets (and related heterostructures) are especially promising for MO devices, owing to their strong magneto-optical activity combined with low losses [2–7]. Strong MO effects also enable information exchange between the photons and the magnetization, via Brillouin light scattering (BLS). BLS is an extremely sensitive probe of magnetization [8,9] with a high spatial and temporal resolution. Such an information exchange is promising for the coveted microwave-to-optical conversion [10–13] since the magnetization couples strongly to microwaves [14–16]. This conversion would require a strong and coherent coupling between the magnetization and optical photons.

This coupling can be boosted by an optical cavity, where the dielectric material is patterned to serve as a resonator [17–21]. Examples include magnetic spheres [22–34], slabs [35], disks [36], waveguides [13, 37, 38], layered structures [29, 39–43], and crystals [44]. Further developments investigate optical cavities with antiferromagnets [45] and magnetized epsilon-near-zero materials [46, 47]. Current work focuses on the design and optimization of optomagnonic systems on the nanoscale [13, 29, 39, 40, 44]. This is an important task to guide future experimental endeavors, since the state-of-the-art coupling strength is far below the predicted theoretical maximum value, mostly due to mode mismatch [23, 25–27, 30, 44].

Due to the complexity of such geometries, the coupling needs to be calculated and optimized numerically. Most calculations however, involve simulation approaches which disregard several physical effects originating from the interaction of the light and the magnetization, e.g. [36, 44]. In particular, magneto-optical effects [48] which stem from the splitting of the atomic energy levels due to the presence of a magnetic field, are not fully considered. A much more powerful approach would be to perform electromagnetic simulations which take the magnetic properties of the material into account. Since the Finite-Difference Time-Domain (FDTD) method [49]

is a broadly applicable and powerful numerical approach for computational electrodynamics, this method seems to be a suitable candidate for this goal. Although such approaches have been already explored in the past to a certain extent [50–53], none of them has been used to explore the effects of the magneto-optical interaction in detail. Furthermore, these approaches cannot be used to perform the very computationally expensive simulations needed for the exploration of large 3D geometries with high resolution. Thus, in this work we extend the in-house FDTD code [54] developed for high performance nanoplasmonic computations to also treat magnetic dielectrics, by implementing the effective permittivity tensor modeling magneto-optical effects. In particular, we explore the Faraday effect.

As a benchmark system, we investigate the plane wave scattering of light on a magnetized sphere in the Mie regime. We choose this problem since it is analytically treatable as we show below, and has also already been investigated using theoretical predictions assisted with numerical tools [33, 34, 55–57]. As a material, we choose the ferrimagnet Yttrium-Iron-Garnet (YIG), the material of choice in optomagnonics due to its good magnetic and optical properties [58, 59].

This work is structured as follows: In section (II) we give a brief introduction to magneto-optical effects and derive the corresponding effective permittivity tensor to be implemented into the FDTD method. Furthermore, we derive the theoretical expressions for the considered scattering problem using basic Mie theory [60] extended to magnetic materials using the effective permittivity tensor. In section (III) we give a brief introduction to the FDTD technique and show how to implement the effective permittivity tensor to extend the FDTD method to treat also magnetic dielectrics. After discussing the simulation approach of our benchmark system in section (IV) we compare the theoretical predictions to the simulation outcome.

2. Mie light scattering of a magnetic sphere

In the following we study the elastic scattering of optical photons impinging on a ferromagnetic sphere in the Mie regime, where the radius of the sphere is comparable to the photon’s wavelength. We consider an incident plane wave polarized along $\hat{\mathbf{x}}$ and propagating along $\hat{\mathbf{z}}$ with the electric field

$$\mathbf{E}_{\text{in}} = E_0 e^{ik_0 z} \hat{\mathbf{x}} \quad (1)$$

The sphere is assumed to be magnetized along $\hat{\mathbf{z}}$ with magnetization

$$\mathbf{M} = M_s \hat{\mathbf{z}} \quad (2)$$

where M_s is the saturation magnetization. We note that this setting represents the so-called Faraday geometry (see Sec 2.1). The electromagnetic fields are governed by Maxwell’s equations (assuming a time dependence $e^{-i\omega t}$)

$$\begin{aligned} \nabla \cdot \mathbf{D} &= 0 \\ \nabla \cdot \mathbf{B} &= 0 \\ \nabla \times \mathbf{E} &= i\omega \mathbf{B} \\ \nabla \times \mathbf{H} &= -i\omega \mathbf{D} \end{aligned} \quad (3)$$

with the magnetizing field $\mathbf{H} = \mathbf{B}/\mu_0$ where μ_0 is the permeability of free space. Outside the sphere, the displacement field is $\mathbf{D} = \mathbf{E}/\varepsilon_0$ with ε_0 the permittivity of free space. Inside the sphere, the permittivity is a magnetization dependent tensor $\mathbf{D}_i = \varepsilon_{ij} \mathbf{E}_j$ which is discussed below (see Sec. 2.1).

Since the incident fields are produced by external sources, they are solutions of Maxwell’s equations which are finite everywhere regardless of the presence of the sphere. These solutions

for a given frequency ω and wave vector $k_0 = \omega/c$ are characterized by the angular indices $\{l, m\}$ and the polarization $\sigma \in \{\text{TE}, \text{TM}\}$. Thus, we can expand any incident field as (see Sup. A.1)

$$\mathbf{E}_{\text{in}}(\mathbf{r}) = \sum_{lm} \frac{1}{k_0 r} \left[\mathcal{E}_{lm}^{\text{in}} \mathbf{E}_{lm,\text{TE}}^{\text{in}}(\mathbf{r}) + c \mathcal{B}_{lm}^{\text{in}} \mathbf{E}_{lm,\text{TM}}^{\text{in}}(\mathbf{r}) \right], \quad (4)$$

where the coefficients $\{\mathcal{E}_{lm}^{\text{in}}, \mathcal{B}_{lm}^{\text{in}}\}$ are the amplitude of TE and TM waves respectively. The eigenmodes are explicitly given by

$$\begin{aligned} \mathbf{E}_{lm,\text{TE}}^{\text{in}}(\mathbf{r}) &= S_l(k_0 r) \mathbf{Y}_l^m(\theta, \phi), \\ \mathbf{E}_{lm,\text{TM}}^{\text{in}}(\mathbf{r}) &= -\sqrt{l(l+1)} \frac{S_l(k_0 r)}{k_0 r} \mathbf{X}_l^m(\theta, \phi) + i S_l'(k_0 r) \mathbf{Z}_l^m(\theta, \phi) \end{aligned} \quad (5)$$

with S_l the Riccati-Bessel functions (see Sup. Eq. [6]) and \mathbf{R}_l^m the vector spherical harmonics (see Sup. Eq. [2]). For a plane wave, the coefficients for the expansion turn out to be (see Sup. A.2)

$$\begin{aligned} \mathcal{E}_{lm}^{\text{in}} &= E_0 \sqrt{\pi(2l+1)} i^l [\delta_{m,1} + \delta_{m,-1}], \\ \mathcal{B}_{lm}^{\text{in}} &= \frac{E_0}{c} \sqrt{\pi(2l+1)} i^{l+1} [\delta_{m,1} - \delta_{m,-1}]. \end{aligned} \quad (6)$$

A similar expansion as in Eq. (4) can be defined for scattered (outgoing) fields

$$\mathbf{E}_{\text{S}}(\mathbf{r}) = \sum_{lm} \frac{1}{k_0 r} \left[\mathcal{E}_{lm}^{\text{S}} \mathbf{E}_{lm,\text{TE}}^{\text{S}}(\mathbf{r}) + c \mathcal{B}_{lm}^{\text{S}} \mathbf{E}_{lm,\text{TM}}^{\text{S}}(\mathbf{r}) \right], \quad (7)$$

with expansion coefficients $\{\mathcal{E}_{lm}^{\text{S}}, \mathcal{B}_{lm}^{\text{S}}\}$. Here, $\mathbf{E}_{lm,\sigma}^{\text{S}}$ are given by replacing $S_l \rightarrow \xi_l$ in Eqs. (5), where ξ_l are outgoing radial waves (see Sup. Eq. [8]). In the remaining section, we derive the scattered coefficients in terms of the incident coefficients.

2.1. Magneto-optical effects

In general, magneto-optical effects [48, 61] refer to changes in the optical polarization states upon interaction with materials that are either subjected to an external magnetic field or magnetically ordered (or both). In all cases, a magnetic field is present, either externally or internally, which causes a splitting of the atomic energy levels in the system with which the light can interact via electric-dipole transitions. This splitting, in general, creates different quantum states with non-degenerate energies and angular momenta. As a consequence, the different polarization states of the light can interact differently with the material, since each polarization state interacts with a different non-degenerate energy level. This leads to optical anisotropy which can be observed as birefringence.

In general, the splitting of the energy levels due to an external field is caused by two main mechanisms: The Zeeman effect [62] which refers to the energy splitting in the presence of an external field and the spin-orbit coupling [63] which refers to the splitting due to the spin-orbit interaction. Which effect is causing the splitting, highly depends on the material. In total, there are two classes of materials and a third representing a transition between the two [64]: (i) Diamagnetic, transparent solids with at least uniaxial symmetry where magneto-optical effects can only be caused by the Zeeman effect. (ii) Paramagnetic and ferromagnetically ordered materials where magneto-optical effects are predominately caused by the spin-orbit coupling which usually exceeds the Zeeman interaction. (iii) Semiconductors and non-ferromagnetic metals represent a transition between the two. Usually, both effects are present and non-negligible.

Considering only the effects affecting the polarization of the transmitted light, magneto-optical effects can be classified into two classes according to the relative orientation of the light wave vector \mathbf{k} with respect to the magnetic field \mathbf{H} : (i) The Faraday geometry with $\mathbf{k} \parallel \mathbf{H}$ and (ii) the Voigt geometry with $\mathbf{k} \perp \mathbf{H}$. In the case of the Faraday geometry, birefringence occurs since the two circularly polarized components of the light effectively see different refractive indices resulting in the so-called magnetic circular birefringence or the Faraday effect. In the case of the Voigt geometry the two linearly polarized components see different refractive indices, causing the so-called magnetic linear birefringence or the Cotton-Mouton/ Voigt effect.

In this work, we focus on the Faraday effect only. As discussed above, due to the magnetic fields present, phenomenologically the two circular polarized components of the linear polarized light see different refractive indices n_+ and n_- what causes them to propagate with different speeds, c/n_+ and c/n_- , through the medium. As a consequence, the two polarization states acquire a phase shift resulting in an overall rotation of a linearly polarized light. The angle of rotation is called the Faraday rotation θ_F which can be expressed as [48]

$$\theta_F = \frac{\omega}{2c}(n_+ - n_-)L \quad (8)$$

with ω the frequency of the light, c the speed of light, and L the propagation length of the light.

For modeling magneto-optical effects we need to introduce an effective permittivity tensor. We note that in general, magneto-optical effects can be entirely modeled by either using the effective permittivity or the effective permeability [64]. However, when working at optical frequencies it is difficult to give clear physical interpretation to the magnetization and thus the permeability [65]. As a consequence, it is common to use the permittivity only and set the permeability to that of vacuum.

In the case of dispersive magnetic materials, the modified effective permittivity due to the Faraday effect is given by (see Sup. B)

$$\bar{\boldsymbol{\varepsilon}}(\mathbf{M}, \omega) = \varepsilon_0 \begin{bmatrix} \varepsilon_r(\omega) & -if_F(\omega)M_z & if_F(\omega)M_y \\ if_F(\omega)M_z & \varepsilon_r(\omega) & -if_F(\omega)M_x \\ -if_F(\omega)M_y & if_F(\omega)M_x & \varepsilon_r(\omega) \end{bmatrix}, \quad (9)$$

where ε_0 is the vacuum permittivity, ε_r the relative permittivity, and f_F is a material dependent constant related to the Faraday rotation via $f_F = [(2c\sqrt{\varepsilon_r})/(\omega M_s)]\theta_F$.

For modeling $\varepsilon_r(\omega)$ and $f_F(\omega)$ we consider a specific dispersion model [46]. Since in magnetic dielectrics, the Faraday effect microscopically originates from electric dipole transitions between degenerate ground and excited states due to the energy splitting e.g. caused by the spin-orbit coupling and the Zeeman interaction [46, 63, 64], our minimal model considers a single-resonance Lorentz-like dispersion model [46]

$$\begin{aligned} \varepsilon_r(\omega) &= 1 + \frac{\omega_0^2(\varepsilon_r - 1)}{\omega_0^2 - \omega^2 - i\eta\omega}, \\ f_F(\omega) &= \frac{A_3\omega\omega_0}{(\omega_0^2 - \omega^2 - i\eta\omega)^2}, \end{aligned} \quad (10)$$

where ω_0 is the resonance frequency for the ionic transitions in the absence of perturbations, ε the permittivity for $\omega \ll \omega_0$, η an absorption factor (required by causality), and A_3 a quantity which depends on the spin-orbit coupling and the electric dipole matrix. We note that this model assumes zero orbital angular momentum of the ground state. Although this model can only be seen as a theoretical toy model since it disregards several resonances of the material, it nonetheless represents an appropriate model for our purposes [46].

2.2. Scattering coefficients of the scattered fields

In the following we consider YIG as the basis material, for which the Faraday rotation per unit length θ_F is smaller than 10^4m^{-1} [66]. Inside a sphere with radius $1 \mu\text{m}$, we expect a rotation of < 0.01 , implying that we can treat the Faraday effect as a perturbation. Thus, up to linear order in f_F , the expansion coefficients in Eq. (7) are

$$\mathcal{E}_{lm}^S = \mathcal{E}_{lm}^M + \mathcal{E}_{lm}^F, \quad (11)$$

where the (unperturbed) Mie scattered light coefficients are (see Sup. A.3)

$$\begin{aligned} \mathcal{E}_{lm}^M(k_0) &= E_0 r_l^E(k_0) \sqrt{\pi(2l+1)} i^l [\delta_{m,1} + \delta_{m,-1}] \\ \mathcal{B}_{lm}^M(k_0) &= \frac{E_0}{c} r_l^B(k_0) \sqrt{\pi(2l+1)} i^{l+1} [\delta_{m,1} - \delta_{m,-1}] \end{aligned} \quad (12)$$

and the expansion coefficients of the Faraday scattered fields are (see Sup. A.4)

$$\begin{aligned} \mathcal{E}_{lm}^F(k_0) &= f E_0 \sqrt{\pi} \left[P_{l-1,1}^E(k_0) \sqrt{2l-1} - M_{l+1,1}^E(k_0) \sqrt{2l+3} \right] i^l [\delta_{m,1} - \delta_{m,-1}] \\ \mathcal{B}_{lm}^F(k_0) &= f \frac{E_0 \sqrt{\pi}}{c} \left[P_{l-1,1}^B(k_0) \sqrt{2l-1} - M_{l+1,1}^B(k_0) \sqrt{2l+3} \right] i^{l-1} [\delta_{m,1} + \delta_{m,-1}] \end{aligned} \quad (13)$$

The expressions for r_l^E , r_l^B , P_{lm}^E , P_{lm}^B , M_{lm}^E , and M_{lm}^B can be found in Sup. A.3 and A.4.

Using the azimuthal dependence of vector spherical harmonics $\mathbf{R}_l^m \propto e^{im\phi}$, we can deduce the ϕ dependence of both scattered fields,

$$\begin{aligned} \mathbf{E}_M &\propto \cos \phi \\ \mathbf{E}_F &\propto \sin \phi, \end{aligned} \quad (14)$$

showing that the Mie and the Faraday scattered field are azimuthally orthogonal. In a Cartesian basis this means, as we see in Fig. 1B, that all field components of the Faraday scattered field are rotated by 90° compared to the field components of the Mie scattered field and that E_x and E_y interchange patterns. This is a result of the polarization rotation through the Faraday effect.

2.3. Scattering efficiency

For deriving the scattering cross-section and the scattering efficiency we also expand the magnetic field into vector spherical harmonics by using the following substitutions

$$\begin{aligned} \mathcal{E}_{lm}^i &\rightarrow \mathcal{B}_{lm}^i \\ c \mathcal{B}_{lm}^i &\rightarrow \frac{\mathcal{E}_{lm}^i}{c} \end{aligned} \quad (15)$$

with $i = [\text{in}, \text{M}, \text{F}]$. In general, the cross-section can be expressed as [67]

$$\sigma_S = \frac{W_S}{I_{\text{in}}} \quad (16)$$

with W_S the energy flux of the scattered light through a certain surface and I_{in} the intensity of the incoming plane wave. In spherical coordinates the energy flux can be found via [67]

$$W_S = \frac{1}{2} \mathcal{R}e \left[\int r^2 \sin \theta d\theta d\phi \left(E_{S\theta} H_{S\phi}^* - E_{S\phi} H_{S\theta}^* \right) \right] \quad (17)$$

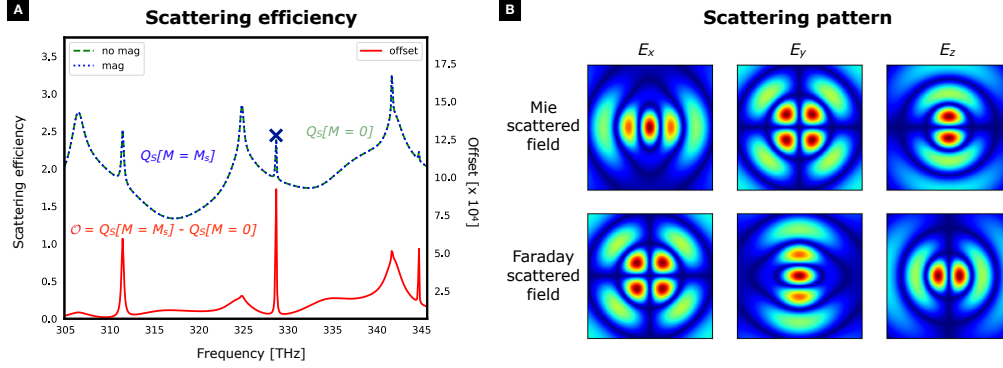


Fig. 1. Light scattering on a magnetic sphere with radius $R = 1 \mu\text{m}$ using Mie theory: (A) Scattering efficiency of a magnetic (blue) and non-magnetic sphere (green) in the frequency range 305 THz to 345 THz. The peaks of the offset $O = Q_S[\mathbf{M} = M_s] - Q_S[\mathbf{M} = 0]$ indicate that the scattering efficiency of the magnetized sphere is broader at the peaks than the scattering efficiency of the un-magnetized sphere which is a result of the energy level splitting of the modes in the presence of a magnetic field. (B) Electric field pattern of the scattered field with frequency 329 THz (wavelength 912.95 nm, identified as TE₁₀, see cross in A) in a plane perpendicular to the propagation direction of the incident wave (xy -plane) in the far field using a Cartesian basis (see Fig. 2B dashed line, $z \sim 3 \mu\text{m}$ measured from the center of the sphere in propagation direction of the incoming wave). The Faraday scattered field components are rotated by 90° compared to the Mie scattered field components and E_x and E_y interchanged patterns which is a direct result of the Faraday rotation. Note: In A and B we used the Lorentz model in Eq. (10) for f_F (average value in the investigated frequency: $f_F = 0.0002$).

with $\mathbf{E}_S = \mathbf{E}_M + \mathbf{E}_F$ and $\mathbf{H}_S = \mathbf{B}_S/\mu_0 = (\mathbf{B}_M + \mathbf{B}_F)/\mu_0$ the total scattered fields. Since the incoming wave is a plane wave, its intensity is given by

$$I_{\text{in}} = \frac{E_0^2}{2\eta} \quad (18)$$

with the impedance $\eta = \sqrt{\mu_0/n^2\epsilon_0}$. Dividing the scattering cross-section by the geometric cross-section of the sphere gives the scattering efficiency

$$Q_S = \frac{\sigma_S}{\sigma_{\text{geom}}} = \frac{\sigma_S}{\pi R^2}. \quad (19)$$

Fig. 1A shows the scattering efficiencies for a magnetized and an un-magnetized sphere in the frequency range 305 THz to 345 THz. For “measuring” their difference, we introduce the following offset measure

$$O = Q_S[\mathbf{M} = M_s] - Q_S[\mathbf{M} = 0] \quad (20)$$

which is also plotted in Fig. 1A. As the peaks of the offset only occur at the scattering peaks, we can deduce that the scattering efficiency of the magnetized sphere is broader at the peaks than the scattering efficiency of the un-magnetized sphere. This is a result of the energy mode splitting. We note that in contrast to [55] we do not observe a splitting of the peaks since we only consider the effects that are linear in f_F whereas the splitting is a second order effect. This is valid because the typical line widths of Mie resonances are larger than the small splittings.

3. FDTD approach for magneto-optical effects

Below we show how the FDTD method can be extended to treat magnetic dispersive media and thus to incorporate magneto-optical effects.

3.1. The FDTD method

The FDTD technique is a numerical method to perform electromagnetic simulations. The success of this method is based on its simplicity combined with its broad applicability especially to many complex materials in arbitrary shape configurations and for broad bandwidths. The FDTD method belongs to the finite difference methods solving the time-dependent Maxwell's equations [68]

$$\begin{aligned}\frac{\partial \mathbf{D}(\mathbf{r}, t)}{\partial t} &= \nabla \times \mathbf{H}(\mathbf{r}, t) - \mathbf{J}_{free}(\mathbf{r}, t), \\ \frac{\partial \mathbf{B}(\mathbf{r}, t)}{\partial t} &= -\nabla \times \mathbf{E}(\mathbf{r}, t),\end{aligned}\tag{21}$$

alongside $\mathbf{D}(\mathbf{r}, t) = \varepsilon_0 \mathbf{E}(\mathbf{r}, t) + \mathbf{P}(\mathbf{r}, t)$ and $\mathbf{H}(\mathbf{r}, t) = 1/\mu_0 \mathbf{B}(\mathbf{r}, t) + \mathbf{M}(\mathbf{r}, t)$. These coupled differential equations are transformed into numerical equations by using the central differencing scheme

$$\frac{df}{dx} = \frac{f(x + h/2) - f(x - h/2)}{h}.\tag{22}$$

Following the so-called Yee algorithm [49], time and space derivatives are substituted by their corresponding central differencing formulas and the simulation domain is discretized with a regular structured rectangular grid. For maintaining second order accuracy of the central differencing operators, the Yee algorithm staggers the electric and magnetic fields in both time and space. This means that in time Maxwell's equations are solved in a leapfrog manner, meaning that first the electric field vector components are solved in a given space region at a given instant of time, then the magnetic field vector components are solved in the same region at the next instant of time. Besides the staggering in time, also the spatial grids of both fields are staggered meaning that the electric field vector components are located midway between a pair of magnetic field vector components. These staggered grids result in the typical FDTD relation: At any given point in space, the updated E-field (H-field) in time depends on the stored value of the E-field (H-field) and the numerical curl of the surrounding H-field (E-field) in space. This nicely represents the given relations in Maxwell's equation where the change of the E-field (H-field) in time is dependent on the spatial change in the H-field (E-field) [49, 68–70].

One big advantage of the FDTD method is that almost any dispersive material can be modeled. Since dispersive media exhibit a frequency dependent susceptibility $\chi(\omega)$, the expression for the susceptibility needs to be known to derive the polarization vector [68]

$$\mathbf{P}(\omega) = \varepsilon_0 \chi(\omega) \mathbf{E}(\omega)\tag{23}$$

which then includes the dispersive material properties via the update equations for the electric field. Thus, for implementing a dispersive material using a model for $\chi(\omega)$ we need to introduce an auxiliary differential equation in the leap frog scheme for the polarization vector \mathbf{P} [68].

3.2. Extension to dispersive magnetic materials

As already mentioned, for implementing a material into the FDTD method the material's susceptibility tensor needs to be known as a function of frequency to adapt the update equations. Since the susceptibility is related to the permittivity via $\chi = \varepsilon - 1$, the frequency dependent susceptibility of a magnetic material can be derived by using the frequency dependent permittivity tensor in Eq. (9) in combination with the introduced single-resonance model in Eq. (10).

For implementing the susceptibility model into the update equations of the electric field we need the polarization vector \mathbf{P} which in our case is given by

$$\mathbf{P} = \varepsilon_0 \frac{\omega_0^2(\varepsilon_r - 1)}{\omega_0^2 - \omega^2 - i\eta\omega} \mathbf{E} + i\omega\varepsilon_0 \frac{A_3\omega_0}{(\omega_0^2 - \omega^2 - i\eta\omega)^2} [\mathbf{M} \times \mathbf{E}]. \quad (24)$$

This equation describes the optical response of a magnetic material in the frequency domain, for transforming it into the time domain we need to apply a Fourier transform (see Sup. C.1) leading to

$$\begin{aligned} \partial_t^4 \mathbf{P} + 2\eta \partial_t^3 \mathbf{P} + (2\omega_0^2 + \eta^2) \partial_t^2 \mathbf{P} + 2\omega_0^2 \eta \partial_t \mathbf{P} + \omega_0^4 \mathbf{P} \\ = \varepsilon_0 \omega_0^2 (\varepsilon - 1) [\partial_t^2 \mathbf{E} + \eta \partial_t \mathbf{E} + \omega_0^2 \mathbf{E}] - \varepsilon_0 A_3 \omega_0 [\mathbf{M} \times \partial_t \mathbf{E}]. \end{aligned} \quad (25)$$

We note that we assumed a slowly varying magnetization \mathbf{M} in time compared to the electric field \mathbf{E} , thus $\partial_t [\mathbf{M} \times \mathbf{E}] = [\mathbf{M} \times \partial_t \mathbf{E}]$. The update equations for the polarization vector are then obtained by using central differencing (see Sup. C.2) which then includes the magnetic model via the update equations for the electric field in the FDTD method.

3.3. Model for YIG

In order to benchmark our numerical method, we consider the material Yttrium-Iron-Garnet, a typical choice for magneto-optical phenomena. For adapting our model to the material parameters of YIG, we need to find the values for the unknown parameters ε , η , and A_3 . Although YIG has several absorption lines between 400 nm and 900 nm (see [58] Fig. 1), the broad and strong absorption line at ~ 500 nm gives a strong contribution to the Faraday effect (see [66] Fig. 2). We therefore set the resonance frequency to $\omega_0 = 2\pi c/\lambda = 2\pi \times 600$ THz which sets the parameters to $\varepsilon_r = 4.9$ and $A_3 \sim -2.25 \cdot 10^{22}$ rad²Hz²m/A [71]. Since we are working with a single-resonance model, the absorption parameter η can be set to the absorption coefficient of YIG $\eta/\omega_0 \sim 10^{-6}$ (@ 1.2 μm) [72]. Note that we use a single frequency ω_0 for benchmarking purposes. For a realistic model of the scattering, all absorption lines within the frequency range of interest should be considered.

4. Benchmarking the extended method

Following the analytical predictions derived in Secs 2.2 and 2.3, we simulate the scattering of a plane wave which is propagating along $\hat{\mathbf{z}}$ and polarized along $\hat{\mathbf{y}}$ on a magnetic YIG sphere with radius $R = 1 \mu\text{m}$ fully magnetized along $\hat{\mathbf{z}}$. Since we want to reconstruct the features stemming from the Faraday effect derived in the theory discussion, our aim is to obtain the scattering efficiency and the scattered mode profile with the extended FDTD code.

4.1. Simulation approach

Since we are simulating a scattering problem, beside the sphere we also need to simulate the air surrounding the sphere which needs to be truncated to a finite domain. Thus, we choose a cubic simulation domain which is subdivided into four regions (see Fig. 2A): (i) the YIG sphere, (ii) the total field region surrounding the sphere and containing all simulated fields, the incident and the scattered fields, (iii) the scattered field region which contains only the scattered fields, and (iv) the convolutional perfectly matched layers (CPML) region which truncate the computational domain to a finite volume but simulating free space by absorbing all outgoing waves. Since the near fields should have decayed before reaching the CPML region, the distance between the sphere surface and the CPML layers should be large enough, ideally $\sim 3\lambda$. Due to computational constraints, we however chose a distance of $\sim 2\lambda$ which should still account for a sufficient decay of the near fields. Assuming the wavelength of the scattered field to be ~ 1000 nm, our

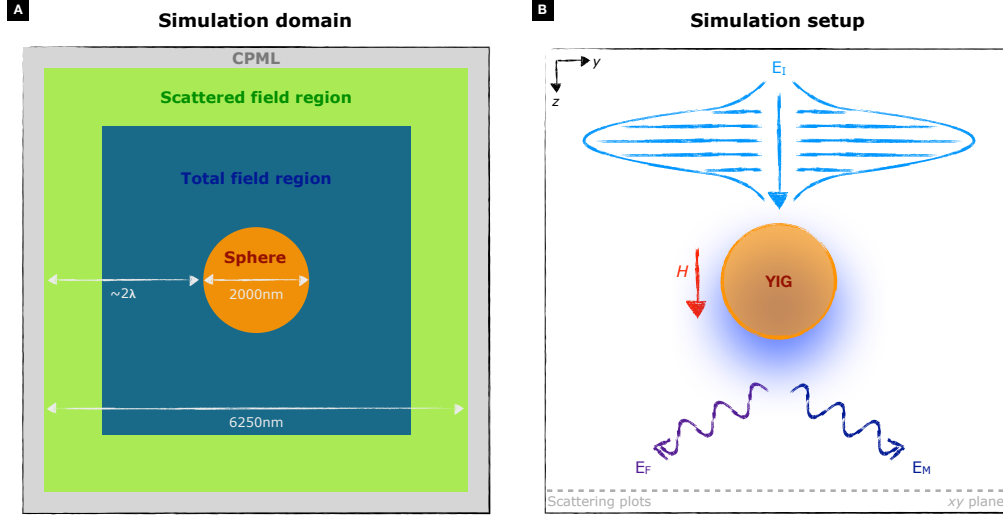


Fig. 2. Simulation domain and setup: (A) Simulation domain consisting of (i) the YIG sphere (red), (ii) the total field region (blue) containing all simulated fields (iii) the scattered field region (green) containing only the scattered fields, and (iv) the convolutional perfectly matched layers (CPML) region (gray) truncating the computational domain to a finite volume (note that the actual simulation domain is 3D). (B) Sketch of the simulation setup. The incident field in the form of a Gaussian plane wave pulse propagates along the magnetization direction of the sphere and is scattered into the Mie and Faraday scattered part. The dashed line indicates the plane the spatial mode shapes were evaluated in Figs. 1 and 3.

simulation domain has a side length of $D = 6250 \text{ nm} \sim 2(R + 2\lambda)$ (excluding the CPML region). For good absorbing effects at the air boundaries the CPML layer is 30 cells thick (regardless of the actual cell size). Furthermore, the total field - scattered field boundary is set to be 40 cells away from the CPML layer (again regardless of the actual cell size).

For discretizing the simulation domain, we use an uniform per-component staircasing grid which assigns the permittivity for each electric field component based on the position of the sampling point in the simulation cell relative to the sphere. This means if the sampling point lies inside the sphere, the permittivity of YIG is assigned, if the point is outside the sphere the permittivity of air is assigned. This is in contrast to a staircase grid where the permittivity is assigned to the whole cell [54]. For avoiding numerical dispersion, we choose a uniform cell size of $\Delta d = 10 \text{ nm} \sim \lambda/100$ giving $625 \times 625 \times 625$ cells to simulate. Using the Courant stability condition [68]

$$\Delta t \leq \frac{1}{c\sqrt{1/\Delta x^2 + 1/\Delta y^2 + 1/\Delta z^2}} \quad (26)$$

with $\Delta x = \Delta y = \Delta z = \Delta d$ the time step is set to $\Delta t = (\Delta d)/(\sqrt{3}c) = 0.2 \text{ fs}$.

For exciting the system and for stimulating scattering we use a electromagnetic plane wave in the form of a Gaussian source

$$\mathcal{G}(t) = \exp\left(-\frac{t^2}{\sigma^2}\right) \cos(2\pi f_0 t) \quad (27)$$

with width $\sigma = 1.97 \times 10^{-11} \text{ s}$ and center frequency $f_0 = 329 \text{ THz}$ ($\lambda_0 = 912.95 \text{ nm}$, frequency of the mode of interest found by “pre”-simulations).

4.2. Benchmark

For benchmarking the code against the theory predictions shown in Fig. 1 we perform simulations for obtaining the scattering efficiency and the spatial field patterns of the scattered fields.

4.2.1. Scattering efficiency

We start with the scattering efficiency which we need to evaluate for a magnetized ($Q_S[\mathcal{M} = M_s]$) and an un-magnetized sphere ($Q_S[\mathcal{M} = 0]$) implemented as [54]

$$Q_S = \frac{\frac{1}{2} \int_S dS \operatorname{Re} [\mathbf{E} \times \mathbf{H}^*] \cdot \hat{\mathbf{n}}}{\frac{1}{2} \operatorname{Re} [\mathbf{E}_{\text{in}} \times \mathbf{H}_{\text{in}}^*] A_{\text{geom}}} \quad (28)$$

being equal to the theory expression in Eq. (19). For both simulations, we evolve the system for 600000 time steps and evaluate the scattering efficiency in the frequency window 305 THz to 346 THz (868 nm to 984 nm) for 401 points.

Fig. 3A shows the two obtained scattering efficiencies and their offset defined in Eq. (20). As we see, the scattering peaks coincide very well with the theoretical prediction shown in Fig. 1A and also have the same order of magnitude. Also in the simulation, the peaks of the offset mostly occur at the scattering peaks, although they are much less pronounced and more noisy compared to the theory prediction. The reason therefore might be that the contribution of the Faraday effect to the scattering is tiny and the precision in the simulation is not large enough. Furthermore, the offset shows negative components which might stem from a slight peak shift in the case of the magnetized sphere compared to the un-magnetized sphere. Again, this could be due to a precision problem. For overcoming this issue, a much finer mesh is necessary, however our computational power and time are limited such that we cannot use a much finer mesh. Nonetheless, we can conclude that we observe a peak broadening in case of a magnetized sphere which is a result of the code taking the energy mode splitting into account. Since YIG has a small Faraday constant, the linewidth of the Mie resonances masks the magnetization-induced mode splitting, compare e.g. with Ref. [55] where the splitting is resolved due to a much larger Faraday rotation constant of the considered material.

4.2.2. Scattered field patterns

For simulating the scattered field patterns we also need to perform two simulations, one for the magnetized ($\mathbf{M} = M_s \hat{z}$) and one for the un-magnetized sphere ($\mathbf{M} = 0$). The simulation in the un-magnetized case then gives the Mie scattered fields $\mathbf{E}_M = \mathbf{E}[\mathbf{M} = 0]$ and the Faraday scattered fields are deduced from both simulations via $\mathbf{E}_F = \mathbf{E}[\mathbf{M} = M_s \hat{z}] - \mathbf{E}[\mathbf{M} = 0]$. For both simulations, we evolve the system for 60000 time steps and evaluate the scattering pattern for the frequency $f_0 = 329$ THz ($\lambda_0 = 912.95$ nm), which is the mode of interest (see Figs. 1A and 3A). The actual scattered field patterns are obtained by monitoring the time evolution of the field in a plane perpendicular to the propagation axis of the incident plane wave located after the sphere (see Fig. 2B dashed line) and performing a running discrete Fourier transformation on the time-dependent fields in this plane. The plane is placed in the 10th last cell layer in air before the CPML layer to monitor the furthest scattered part of the light. We note that for these simulations we use less time steps compared to the simulations performed for the scattering efficiencies since the weak Faraday scattered fields are "hidden" behind the stronger Mie scattering fields which are much longer present. Furthermore, the FDTD method accumulates a larger error for longer evolution times which also might hide the small contribution of the Faraday scattered field part.

Fig. 3B shows the obtained scattering profiles for the Mie and Faraday scattered field components for the desired scattered mode. As we see, the Mie scattered fields almost resemble the shape of the theory prediction shown in Fig. 1B, however their shape seems to be more "zoomed" in. The reason therefore might be that the theory gives the real far fields whereas

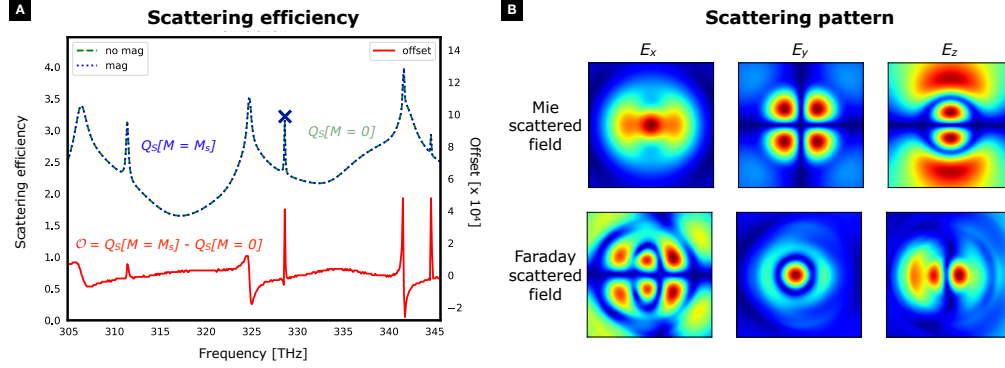


Fig. 3. Light scattering on a magnetic sphere with radius $R = 1 \mu\text{m}$ using the adapted FDTD code: (A) Scattering efficiency of a magnetic (blue) and non-magnetic sphere (green) in the frequency range 305 THz to 345 THz. The peaks of the offset $O = Q_S[M = M_S] - Q_S[M = 0]$ indicate that the scattering efficiency of the magnetized sphere is broader at the peaks than the scattering efficiency of the un-magnetized sphere which is a result of the splitting of the modes in the presence of a magnetic field. The reason for less pronounced peaks and negative contributions are precision issues in the simulation (B) Electric field pattern of the scattered field with frequency 329 THz (wavelength 912.95 nm, identified as TE₁₀, see cross in A) in a plane perpendicular to the propagation direction of the incident wave (xy -plane) in the far field using a Cartesian basis (see Fig. 2B dashed line, $z \sim 3 \mu\text{m}$ measured from the center of the sphere in propagation direction of the incoming wave). The Faraday scattered field components are rotated by 90° compared to the Mie scattered field components and E_x and E_y interchanged patterns which is a direct result of the Faraday rotation.

the simulation outcome shows the near and intermediate fields since the simulation domain is truncated. Although the obtained Faraday scattered fields are much more noisy, they still show the expected behavior: The E_z component is rotated by 90° and the E_x and E_y component interchanged shape. The reason for the noisy shape for the E_x component might be that this component has the smallest contribution in absolute value and thus the actual shape might be hidden behind noise. For overcoming this issue, we also need to use a finer mesh and to increase the simulation domain such that we can evaluate the patterns in the real far field. Furthermore, a longer simulation time is required to resolve the sharp resonances. As already mentioned, this is limited by the available computational power and time constrains. Nonetheless, we can conclude that the code correctly obtains the rotation stemming from the Faraday rotation.

5. Conclusion

We proposed an approach to extend the FDTD method to treat magnetic dispersive media by using a modified effective permittivity encapsulating the Faraday effect. As a benchmark system to test the functionality of the extended method, we considered the scattering of a plane wave on a fully magnetized YIG sphere in the Mie regime. We theoretically showed that including the modified effective permittivity in Maxwell's equations results in broadened peaks in the scattering efficiency nicely showing the splitting of atomic energy levels when a magnetic field is present. Furthermore, the scattered fields include an additional part rotated with respect to the usual Mie scattered fields stemming from the light-matter interaction through the Faraday effect

We showed that the extended FDTD method can reproduce both predicted features: the peak broadening in the scattering efficiency and the rotation in the scattered fields. These features are not as pronounced as in the analytical model due to the high Q of the considered modes,

which are hard to resolve within FDTD. For better results a higher resolution in space and longer simulation times are necessary, which is not feasible with our current computational resources. For benchmarking the system further, other frequency ranges where the Faraday effect is more pronounced could be explored. However, higher frequencies have even higher Q and thus, are harder to simulate using the FDTD method.

A possible field of application for the extended method might be magnetoplasmonics where the interaction of plasmonics and magneto-optical effects is explored. In this context, an Epsilon-Near-Zero (ENZ) optomagnonic structure, as proposed e.g. in [46], could be investigated which serves as an additional route to enhance the optomagnonic coupling. Furthermore, backaction in the optomagnonic coupling could be explored.

6. Acknowledgments

We thank Victor Bittencourt and Jesse Thompson for insightful discussions. This research was performed as part of a collaboration within the Max Planck-University of Ottawa Centre for Extreme and Quantum Photonics, whose support all authors gratefully acknowledge. J.G. acknowledges financial support from the Max Planck-uOttawa Center for Extreme and Quantum Photonics and from the International Max Planck Research School - Physics of Light (IMPRS-PL). J.G. also acknowledges support from the Visiting Student Researcher Program at the uOttawa. J. G. and S.V.K. acknowledge funding from the Deutsche Forschungsgemeinschaft (DFG, German Research Foundation) through ProjectID 429529648–TRR 306 QuCoLiMa (“Quantum Cooperativity of Light and Matter”). J.B. and L.R. acknowledge funding from the Vanier Canada Graduate Scholarships program (NSERC) and the computational resources and support of the Digital Research Alliance of Canada.

References

1. A. Kimel, A. Zvezdin, S. Sharma, S. Shallcross, N. de Sousa, A. García-Martín, G. Salvan, J. Hamrle, O. Stejskal, J. McCord, S. Tacchi, G. Carlotti, P. Gambardella, G. Salis, M. Müntenberg, M. Schultze, V. Temnov, I. V. Bychkov, L. N. Kotov, N. Maccaferri, D. Ignatyeva, V. Belotelov, C. Donnelly, A. H. Rodríguez, I. Matsuda, T. Ruchon, M. Fanciulli, M. Sacchi, C. R. Du, H. Wang, N. P. Armitage, M. Schubert, V. Darakchieva, B. Liu, Z. Huang, B. Ding, A. Berger, and P. Vavassori, “The 2022 magneto-optics roadmap,” *J. Phys. D: Appl. Phys.* **55**, 463003 (2022).
2. C. Rizal, H. Shimizu, and J. R. Mejía-Salazar, “Magneto-Optics Effects: New Trends and Future Prospects for Technological Developments,” *Magnetochemistry* **8**, 94 (2022).
3. W.-K. Li and G.-Y. Guo, “First-principles study on magneto-optical effects in the ferromagnetic semiconductors $y_3fe_5o_{12}$ and $bi_3fe_5o_{12}$,” *Phys. Rev. B* **103**, 014439 (2021).
4. M. C. Onbasli, L. Beran, M. Zahradník, M. Kučera, R. Antoš, J. Mistrík, G. F. Dionne, M. Veis, and C. A. Ross, “Optical and magneto-optical behavior of Cerium Yttrium Iron Garnet thin films at wavelengths of 200–1770 nm,” *Sci. Reports* **6**, 23640 (2016).
5. N. Zhu, X. Zhang, X. Han, C.-L. Zou, and H. X. Tang, “Inverse Faraday Effect in an Optomagnonic Waveguide,” *Phys. Rev. Appl.* **18**, 024046 (2022).
6. T. Fakhrol, S. Tazlaru, L. Beran, Y. Zhang, M. Veis, and C. A. Ross, “Magneto-Optical Bi:YIG Films with High Figure of Merit for Nonreciprocal Photonics,” *Adv. Opt. Mater.* **7**, 1900056 (2019). [_eprint: https://onlinelibrary.wiley.com/doi/pdf/10.1002/adom.201900056](https://onlinelibrary.wiley.com/doi/pdf/10.1002/adom.201900056).
7. M. Nur-E-Alam, M. Vasiliev, and K. Alameh, “Bi-Substituted Ferrite Garnet Type Magneto-Optic Materials Studied at ESRI Nano-Fabrication Laboratories, ECU, Australia,” *Coatings* **12**, 1471 (2022).
8. A. Borovik-Romanov and N. Kreines, “Brillouin-mandelstam scattering from thermal and excited magnons,” *Phys. Reports* **81**, 351–408 (1982).
9. T. Sebastian, K. Schultheiss, B. Obry, B. Hillebrands, and H. Schultheiss, “Micro-focused brillouin light scattering: imaging spin waves at the nanoscale,” *Front. Phys.* **3** (2015).
10. R. Hisatomi, A. Osada, Y. Tabuchi, T. Ishikawa, A. Noguchi, R. Yamazaki, K. Usami, and Y. Nakamura, “Bidirectional conversion between microwave and light via ferromagnetic magnons,” *Phys. Rev. B* **93**, 174427 (2016).
11. D. Lachance-Quirion, Y. Tabuchi, A. Gloppe, K. Usami, and Y. Nakamura, “Hybrid quantum systems based on magnonics,” *Appl. Phys. Express* **12**, 070101 (2019).
12. F. Engelhardt, V. A. S. V. Bittencourt, H. Huebl, O. Klein, and S. V. Kusminskiy, “Optimal broad-band frequency conversion via a magnomechanical transducer,” *arXiv:2205.05088v2* (2022).
13. N. Zhu, X. Zhang, X. Han, C.-L. Zou, C. Zhong, C.-H. Wang, L. Jiang, and H. X. Tang, “Waveguide cavity optomagnonics for microwave-to-optics conversion,” *Optica* **7**, 1291–1297 (2020).

14. Y. Tabuchi, S. Ishino, A. Noguchi, T. Ishikawa, R. Yamazaki, K. Usami, and Y. Nakamura, "Coherent coupling between a ferromagnetic magnon and a superconducting qubit," *Science* **349**, 405–408 (2015).
15. X. Zhang, C.-L. Zou, L. Jiang, and H. X. Tang, "Strongly coupled magnons and cavity microwave photons," *Phys. Rev. Lett.* **113**, 156401 (2014).
16. J. A. Haigh, N. J. Lambert, A. C. Doherty, and A. J. Ferguson, "Dispersive readout of ferromagnetic resonance for strongly coupled magnons and microwave photons," *Phys. Rev. B* **91**, 104410 (2015).
17. S. V. Kusminskiy, "Cavity optomagnonics," arXiv:1911.11104 (2019).
18. S. Viola Kusminskiy, H. X. Tang, and F. Marquardt, "Coupled spin-light dynamics in cavity optomagnonics," *Phys. Rev. A* **94**, 033821 (2016).
19. R. Hisatomi, A. Noguchi, R. Yamazaki, Y. Nakata, A. Gloppe, Y. Nakamura, and K. Usami, "Helicity-changing brillouin light scattering by magnons in a ferromagnetic crystal," *Phys. Rev. Lett.* **123**, 207401 (2019).
20. V. A. S. V. Bittencourt, V. Feulner, and S. V. Kusminskiy, "Magnon heralding in cavity optomagnonics," *Phys. Rev. A* **100**, 013810 (2019).
21. S. Sharma, B. Z. Rameshti, Y. M. Blanter, and G. E. W. Bauer, "Optimal mode matching in cavity optomagnonics," *Phys. Rev. B* **99**, 214423 (2019).
22. S. Sharma, Y. M. Blanter, and G. E. W. Bauer, "Light scattering by magnons in whispering gallery mode cavities," *Phys. Rev. B* **96**, 094412 (2017).
23. A. Osada, R. Hisatomi, A. Noguchi, Y. Tabuchi, R. Yamazaki, K. Usami, M. Sadgrove, R. Yalla, M. Nomura, and Y. Nakamura, "Cavity optomagnonics with spin-orbit coupled photons," *Phys. Rev. Lett.* **116**, 223601 (2016).
24. A. Osada, A. Gloppe, Y. Nakamura, and K. Usami, "Orbital angular momentum conservation in brillouin light scattering within a ferromagnetic sphere," *New J. Phys.* **20**, 103018 (2018).
25. A. Osada, A. Gloppe, R. Hisatomi, A. Noguchi, R. Yamazaki, M. Nomura, Y. Nakamura, and K. Usami, "Brillouin light scattering by magnetic quasivortices in cavity optomagnonics," *Phys. Rev. Lett.* **120**, 133602 (2018).
26. J. A. Haigh, A. Nunnenkamp, A. J. Ramsay, and A. J. Ferguson, "Triple-resonant brillouin light scattering in magneto-optical cavities," *Phys. Rev. Lett.* **117**, 133602 (2016).
27. J. A. Haigh, N. J. Lambert, S. Sharma, Y. M. Blanter, G. E. W. Bauer, and A. J. Ramsay, "Selection rules for cavity-enhanced brillouin light scattering from magnetostatic modes," *Phys. Rev. B* **97**, 214423 (2018).
28. J. A. Haigh, S. Langenfeld, N. J. Lambert, J. J. Baumberg, A. J. Ramsay, A. Nunnenkamp, and A. J. Ferguson, "Magneto-optical coupling in whispering-gallery-mode resonators," *Phys. Rev. A* **92**, 063845 (2015).
29. J. Haigh, R. Chakalov, and A. Ramsay, "Subpicoliter magnetooptical cavities," *Phys. Rev. Appl.* **14**, 044005 (2020).
30. X. Zhang, N. Zhu, C.-L. Zou, and H. X. Tang, "Optomagnonic whispering gallery microresonators," *Phys. Rev. Lett.* **117**, 123605 (2016).
31. D. Lachance-Quirion, Y. Tabuchi, S. Ishino, A. Noguchi, T. Ishikawa, R. Yamazaki, and Y. Nakamura, "Resolving quanta of collective spin excitations in a millimeter-sized ferromagnet," *Sci. Adv.* **3**, e1603150 (2017).
32. V. Wachter, V. A. S. V. Bittencourt, S. Xie, S. Sharma, N. Joly, P. S. Russell, F. Marquardt, and S. V. Kusminskiy, "Optical signatures of the coupled spin-mechanics of a levitated magnetic microparticle," *J. Opt. Soc. Am. B* **38**, 3858–3871 (2021).
33. E. Almpanis, "Dielectric magnetic microparticles as photomagnonic cavities: Enhancing the modulation of near-infrared light by spin waves," *Phys. Rev. B* **97**, 184406 (2018).
34. E. Almpanis, G. P. Zouros, P. A. Pantazopoulos, K. L. Tsakmakidis, N. Papanikolaou, and N. Stefanou, "Spherical optomagnonic microresonators: Triple-resonant photon transitions between zeeman-split mie modes," *Phys. Rev. B* **101**, 054412 (2020).
35. T. Liu, X. Zhang, H. X. Tang, and M. E. Flatté, "Optomagnonics in magnetic solids," *Phys. Rev. B* **94**, 060405(R) (2016).
36. J. Graf, H. Pfeifer, F. Marquardt, and S. Viola Kusminskiy, "Cavity optomagnonics with magnetic textures: Coupling a magnetic vortex to light," *Phys. Rev. B* **98**, 241406(R) (2018).
37. N. Zhu, X. Zhang, X. Han, C.-L. Zou, and H. X. Tang, "Inverse faraday effect in an optomagnonic waveguide," *Phys. Rev. Appl.* **18**, 024046 (2022).
38. T. Yu, X. Zhang, S. Sharma, Y. M. Blanter, and G. E. W. Bauer, "Chiral coupling of magnons in waveguides," *Phys. Rev. B* **101**, 094414 (2020).
39. P. A. Pantazopoulos, N. Stefanou, E. Almpanis, and N. Papanikolaou, "Photomagnonic nanocavities for strong light–spin-wave interaction," *Phys. Rev. B* **96**, 104425 (2017).
40. P.-A. Pantazopoulos, N. Papanikolaou, and N. Stefanou, "Tailoring coupling between light and spin waves with dual photonic–magnonic resonant layered structures," *J. Opt.* **21**, 015603 (2018).
41. J. A. Haigh, A. Nunnenkamp, and A. J. Ramsay, "Polarization dependent scattering in cavity optomagnonics," *Phys. Rev. Lett.* **127**, 143601 (2021).
42. P. A. Pantazopoulos, K. L. Tsakmakidis, E. Almpanis, G. P. Zouros, and N. Stefanou, "High-efficiency triple-resonant inelastic light scattering in planar optomagnonic cavities," *New J. Phys.* **21**, 095001 (2019).
43. P.-A. Pantazopoulos, N. Stefanou, E. Almpanis, and N. Papanikolaou, "Simultaneous localization of light and spin waves in dielectric magnetic layered structures for enhanced photon-magnon interaction," in *Advanced Photonics 2018 (BGPP, IPR, NP, NOMA, Sensors, Networks, SPCCOM, SOF)*, (Optica Publishing Group, 2018), p. NoM3J.6.
44. J. Graf, S. Sharma, H. Huebl, and S. V. Kusminskiy, "Design of an optomagnonic crystal: Towards optimal magnon-photon mode matching at the microscale," *Phys. Rev. Res.* **3**, 013277 (2021).

45. T. S. Parvini, V. A. S. V. Bittencourt, and S. V. Kusminskiy, "Antiferromagnetic cavity optomagnonics," *Phys. Rev. Res.* **2**, 022027 (2020).
46. V. A. S. V. Bittencourt, I. Liberal, and S. Viola Kusminskiy, "Optomagnonics in dispersive media: Magnon-photon coupling enhancement at the epsilon-near-zero frequency," *Phys. Rev. Lett.* **128**, 183603 (2022).
47. V. A. S. V. Bittencourt, I. Liberal, and S. Viola Kusminskiy, "Light propagation and magnon-photon coupling in optically dispersive magnetic media," *Phys. Rev. B* **105**, 014409 (2022).
48. A. Zvezdin and V. Kotov, *Modern Magneto-optics and Magneto-optical Materials*, Studies in Condensed Matter Physics (Taylor & Francis Group, 1997).
49. K. Yee, "Numerical solution of initial boundary value problems involving maxwell's equations in isotropic media," *IEEE Trans. on Antennas Propag.* **14**, 302–307 (1966).
50. <https://meep.readthedocs.io/en/latest/Materials/> (accessed October 21, 2022).
51. Y. Law and J. Nave, "High-order FDTD schemes for Maxwell's interface problems with discontinuous coefficients and complex interfaces based on the Correction Function Method," arXiv:2101.05417v2 (2022).
52. L. A. Benali, A. Tribak, J. Terhzaz, and A. Mediavilla, "Characterization of magneto-dielectric materials by a rectangular waveguide using the 2d-fdtd method," *Int. journal microwave optical technology* **16** (2021).
53. B. R. Poole, S. D. Nelson, and S. Langdon, "Advanced electric and magnetic material models for fdtd electromagnetic codes," *IEEE Proceedings of 2005 Particle Accelerator Conference, Knoxville, Tennessee* (2005).
54. A. C. Lesina, A. Vaccari, P. Berini, and L. Ramunno, "On the convergence and accuracy of the fdtd method for nanoplasmonics," *Opt. Express* **23**, 10481–10497 (2015).
55. G. P. Zouros, "Eigenfrequencies and modal analysis of uniaxial, biaxial, and gyroelectric spherical cavities," *IEEE Trans. on Microw. Theory Tech.* **65**, 20–27 (2017).
56. G. P. Zouros and G. C. Kokkorakis, "Electromagnetic scattering by an inhomogeneous gyroelectric sphere using volume integral equation and orthogonal dini-type basis functions," *IEEE Trans. on Antennas Propag.* **63**, 2665–2676 (2015).
57. D. Lacoste, B. A. van Tiggelen, G. L. J. A. Rikken, and A. Sparenberg, "Optics of a faraday-active mie sphere," *J. Opt. Soc. Am. A* **15**, 1636–1642 (1998).
58. G. B. Scott, D. E. Lacklison, and J. L. Page, "Absorption spectra of $Y_3Fe_5O_{12}$ (YIG) and $Y_3Ga_5O_{12}: Fe^{3+}$," *Phys. Rev. B* **10**, 971–986 (1974).
59. V. Cherepanov, I. Kolokolov, and V. L'vov, "The saga of yig: Spectra, thermodynamics, interaction and relaxation of magnons in a complex magnet," *Phys. Reports* **229**, 81 – 144 (1993).
60. G. Mie, "Beiträge zur optik trüber medien, speziell kolloidaler metallösungen," *Ann. der Physik* **330**, 377–445 (1908).
61. P. S. Pershan, "Magneto-optical effects," *J. Appl. Phys.* **38**, 1482–1490 (1967).
62. D. P. Zeeman, "Xxxii. on the influence of magnetism on the nature of the light emitted by a substance," *The London, Edinburgh, Dublin Philos. Mag. J. Sci.* **43**, 226–239 (1897).
63. P. A. Fleury and R. Loudon, "Scattering of light by one- and two-magnon excitations," *Phys. Rev.* **166**, 514–530 (1968).
64. P. S. Pershan, "Magneto-Optical Effects," *J. Appl. Phys.* **38**, 1482–1490 (2004).
65. D. D. Stancil and A. Prabhakar, *Spin waves* (Springer, 2009), 1st ed.
66. W. Wuttling, "Magneto-optics of ferrites," *J. Magn. Magn. Mater.* **3**, 147–160 (1976).
67. C. Bohren and D. Huffman, *Absorbtion and Scattering of Light by Small Particles* (Wiley-VCH Verlag GmbH & Co. KGaA, 2004), 2nd ed.
68. B. D. Bartolo, L. Silvestri, M. Cesaria, and J. Collins, *Quantum Nano-Photonics*, NATO Science for Peace and Security Series B: Physics and Biophysics (Springer, 2017).
69. S. D. Gedney, *Introduction to the Finite-Difference Time-Domain (FDTD) Method for Electromagnetics* (Springer, 2022).
70. J. B. Schneider, "Understanding the finite-difference time-domain method," www.eecs.wsu.edu/~schneidj/ufdtd (2010).
71. W. A. Crossley, R. W. Cooper, J. L. Page, and R. P. van Stapele, "Faraday rotation in rare-earth iron garnets," *Phys. Rev.* **181**, 896–904 (1969).
72. V. A. S. V. Bittencourt, I. Liberal, and S. V. Kusminskiy, "Optomagnonics in dispersive media: magnon-photon coupling enhancement at the epsilon-near-zero frequency," arXiv:2110.02984 (2021).

Supplemental material

A. Light scattering on a magnetic sphere

In the following we provide additional derivations for the light scattering on a magnetic sphere as discussed in the main text.

A.1. Field expansion

All electromagnetic fields $\mathbf{F} \in \{\mathbf{E}, \mathbf{B}, \mathbf{D}, \mathbf{H}\}$ can be expanded as

$$\mathbf{F}(\mathbf{r}) = \sum_{lm} \frac{1}{r} \left[\mathcal{F}_{lm}^X(r) \mathbf{X}_l^m(\theta, \phi) + \mathcal{F}_{lm}^Y(r) \mathbf{Y}_l^m(\theta, \phi) + \mathcal{F}_{lm}^Z(r) \mathbf{Z}_l^m(\theta, \phi) \right], \quad (29)$$

where \mathbf{R}_l^m are the vector spherical harmonics given by

$$\begin{aligned} \mathbf{X}_l^m(\theta, \phi) &= Y_l^m(\theta, \phi) \hat{\mathbf{r}}, \\ \mathbf{Y}_l^m(\theta, \phi) &= \frac{1}{\sqrt{l(l+1)}} \mathbf{L} Y_l^m(\theta, \phi) \\ &= \frac{i}{\sqrt{l(l+1)}} \left[\frac{1}{\sin \theta} \partial_\phi Y_l^m(\theta, \phi) \hat{\boldsymbol{\theta}} - \partial_\theta Y_l^m(\theta, \phi) \hat{\boldsymbol{\phi}} \right], \\ \mathbf{Z}_l^m(\theta, \phi) &= \frac{ir}{\sqrt{l(l+1)}} \nabla Y_l^m(\theta, \phi) \\ &= \frac{i}{\sqrt{l(l+1)}} \left[\partial_\theta Y_l^m(\theta, \phi) \hat{\boldsymbol{\theta}} + \frac{1}{\sin \theta} \partial_\phi Y_l^m(\theta, \phi) \hat{\boldsymbol{\phi}} \right] \end{aligned} \quad (30)$$

with Y_l^m the spherical harmonics. Note that the factor $1/r$ is taken out of the expansion to account for far field radiation. Furthermore, we note that with this field expansion we are now working in spherical coordinates $\mathbf{r} = (r, \theta, \phi)$. Each of these components can be found using the orthonormality relation of the vector spherical harmonics

$$F_{lm}^Y(r) = r \int \sin \theta d\theta d\phi \mathbf{F}(\mathbf{r}) \cdot [\mathbf{V}_l^m(\theta, \phi)]^*. \quad (31)$$

Inserting the expansion in Eq. (29) in Maxwell's equations (Eq. (3) in the main text) gives an independent set of equations for each $\{l, m\}$ pair

$$\begin{aligned} D_{lm}^Y(r) &= \frac{1}{\omega \mu_0} \left[\frac{\sqrt{l(l+1)} B_{lm}^X(r)}{r} - i \frac{dB_{lm}^Z(r)}{dr} \right] \\ B_{lm}^X(r) &= \frac{\sqrt{l(l+1)} E_{lm}^Y(r)}{\omega r} \\ B_{lm}^Z(r) &= \frac{-i}{\omega} \frac{dE_{lm}^Y(r)}{dr} \\ B_{lm}^Y(r) &= -\frac{1}{\omega} \left[\frac{\sqrt{l(l+1)} E_{lm}^X(r)}{r} - i \frac{dE_{lm}^Z(r)}{dr} \right] \\ D_{lm}^X(r) &= -\frac{\sqrt{l(l+1)} B_{lm}^Y(r)}{\omega \mu_0 r} \\ D_{lm}^Z(r) &= \frac{i}{\omega \mu_0} \frac{dB_{lm}^Y(r)}{dr}. \end{aligned} \quad (32)$$

Outside the sphere the permittivity is isotropic and Maxwell's equations further split into two independent sets of equations, one for $\{E_{lm}^Y, B_{lm}^X, B_{lm}^Z\}$ and one for $\{B_{lm}^Y, E_{lm}^X, E_{lm}^Z\}$. Outside the sphere both $E_{lm}^Y(r)$ and $B_{lm}^Y(r)$, satisfy,

$$\frac{d^2 F}{dr^2} + \left(k_0^2 - \frac{l(l+1)}{r^2} \right) F = 0 \quad (33)$$

with $k_0 = \omega/c$. This expression has two independent solutions known as Riccati-Bessel functions, $S_l(k_0 r)$ and $C_l(k_0 r)$, which are related to the Bessel functions via

$$\begin{aligned} S_l(x) &= \sqrt{\frac{\pi x}{2}} J_{l+\frac{1}{2}}(x), \\ C_l(x) &= -\sqrt{\frac{\pi x}{2}} Y_{l+\frac{1}{2}}(x). \end{aligned} \quad (34)$$

While S_l is finite everywhere, C_l diverges at the origin. The linear combinations

$$\begin{aligned} \xi_l(x) &= S_l(x) - iC_l(x) \\ \zeta_l(x) &= S_l(x) + iC_l(x) \end{aligned} \quad (35)$$

as $x \rightarrow \infty$ satisfy the relations

$$\begin{aligned} \xi_l(x) &\propto e^{+ix}, \\ \zeta_l(x) &\propto e^{-ix}. \end{aligned} \quad (36)$$

Consequently, they can be interpreted as outgoing and incoming waves. Given E_{lm}^Y and B_{lm}^Y , the other components can be found from Eqs. (32). The two sets of eigensolutions are labelled as TE (transverse electric) and TM (transverse magnetic). They are given by,

$$\begin{aligned} \mathbf{E}_{lm,TE} &= \frac{R_l(k_0 r)}{k_0 r} \mathbf{Y}_l^m(\theta, \phi) \\ \mathbf{E}_{lm,TM} &= \frac{c}{k_0 r} \left[-\sqrt{l(l+1)} \frac{R_l(k_0 r)}{k_0 r} \mathbf{X}_l^m(\theta, \phi) + iR_l'(k_0 r) \mathbf{Z}_l^m(\theta, \phi) \right], \end{aligned} \quad (37)$$

where $R_l(k_0 r)$ can be any linear combination of S_l and C_l . The magnetic field is given by $TE \leftrightarrow TM$, $\mathbf{E} \rightarrow \mathbf{B}$, and $c \rightarrow -1/c$.

A.2. Incident and scattered fields

The incident field should be finite everywhere as it is generated by an external source far from the sphere, so it can be modelled as the linear combination given in Eq. (4) of the main text,

$$\mathbf{E}_{in}(\mathbf{r}) = \sum_{lm} \frac{1}{k_0 r} \left[\mathcal{E}_{lm}^{in} \mathbf{E}_{lm,TE}^{in} + c \mathcal{B}_{lm}^{in} \mathbf{E}_{lm,TM}^{in} \right], \quad (38)$$

for an arbitrary set of coefficients $\{\mathcal{E}, \mathcal{B}\}$ and $\mathbf{E}^{in} = k_0 r \mathbf{E}$ in terms of Eqs. (37) with $R_l \rightarrow S_l$.

The scattered field is given by an analogous expansion with $\mathcal{E}^{in} \rightarrow \mathcal{E}^S$ and $R_l \rightarrow \xi_l$ to model outgoing waves.

A.3. Mie scattered fields

When $f_F = 0$, there is no Faraday rotation, and the problem reduces to Mie scattering. In the above notation, $\mathcal{E}_{lm}^S = \mathcal{E}_{lm}^M$. In that case, the fields inside the sphere also satisfy Eq. (33) but with $k_0 \rightarrow k = nk_0$ where n is the refractive index. Thus, the fields inside the sphere ($r < R$) are given by an expansion analogous to Eq. (38) with $\mathcal{E}^{\text{in}} \rightarrow \mathcal{E}^{\text{sp}}$ and $k_0 \rightarrow k$. The coefficients can be found using the continuity of $\{D_{lm}^X, E_{lm}^Y, E_{lm}^Z, B_{lm}^X, B_{lm}^Y, B_{lm}^Z\}$ for each lm at the boundary. Explicitly,

$$\begin{aligned}\mathcal{E}_l^{\text{sp}} S_l(nk_0 R) &= \mathcal{E}_l^{\text{in}} S_l(k_0 R) + \mathcal{E}_l^M \xi_l(k_0 R) \\ k \mathcal{E}_l^{\text{sp}} S'_l(nk_0 R) &= k_0 \mathcal{E}_l^{\text{in}} S'_l(k_0 R) + k_0 \mathcal{E}_l^M \xi'_l(k_0 R) \\ \mathcal{B}_l^{\text{sp}} S_l(nk_0 R) &= \mathcal{B}_l^{\text{in}} S_l(k_0 R) + \mathcal{B}_l^M \xi_l(k_0 R) \\ \frac{k}{\epsilon} \mathcal{B}_l^{\text{sp}} S'_l(nk_0 R) &= \frac{k_0}{\epsilon_0} \mathcal{B}_l^{\text{in}} S'_l(k_0 R) + \frac{k_0}{\epsilon_0} \mathcal{B}_l^M \xi'_l(k_0 R).\end{aligned}\tag{39}$$

Using the identity $S_l(x)\xi'_l(x) - S'_l(x)\xi_l(x) = i$ the excitation amplitude turns out to be

$$\begin{aligned}\frac{\mathcal{E}_l^{\text{sp}}}{\mathcal{E}_l^{\text{in}}} &= \frac{i}{S_l(nk_0 R)\xi'_l(k_0 R) - nS'_l(nk_0 R)\xi_l(k_0 R)} \triangleq \chi_l^E \\ \frac{\mathcal{B}_l^{\text{sp}}}{\mathcal{B}_l^{\text{in}}} &= \frac{i}{S_l(nk_0 R)\xi'_l(k_0 R) - n^{-1}S'_l(nk_0 R)\xi_l(k_0 R)} \triangleq \chi_l^B,\end{aligned}\tag{40}$$

where χ can be interpreted as susceptibility. The radiation amplitude of the Mie scattered field is given by

$$\begin{aligned}\frac{\mathcal{E}_l^M}{\mathcal{E}_l^{\text{in}}} &= \frac{nS'_l(nk_0 R)S_l(k_0 R) - S'_l(k_0 R)S_l(nk_0 R)}{S_l(nk_0 R)\xi'_l(k_0 R) - nS'_l(nk_0 R)\xi_l(k_0 R)} \triangleq r_l^E \\ \frac{\mathcal{B}_l^M}{\mathcal{B}_l^{\text{in}}} &= \frac{n^{-1}S'_l(nk_0 R)S_l(k_0 R) - S'_l(k_0 R)S_l(nk_0 R)}{S_l(nk_0 R)\xi'_l(k_0 R) - n^{-1}S'_l(nk_0 R)\xi_l(k_0 R)} \triangleq r_l^B.\end{aligned}\tag{41}$$

We note that the polarization and the angular momentum are preserved in an isotropic scattering process.

A.4. Faraday scattered fields

When $f_F \neq 0$, the scattered light can be written as $\mathcal{E}_{lm}^S = \mathcal{E}_{lm}^M + \mathcal{E}_{lm}^F$, where \mathcal{E}_{lm}^M was found in the previous subsection. For a sphere of radius $1 \mu\text{m}$ and typical Faraday rotation of $< 1 \text{ deg}/\mu\text{m}$, the Faraday effect is a small perturbation. In this section, we find the leading order contribution to the scattered light due to Faraday rotation. As we show below, the Mie scattered component is largely unaffected except for a small renormalization of susceptibility χ , and the Faraday effect inverts the polarization, i.e. we can write

$$\begin{aligned}\mathcal{B}_{lm}^F &= \frac{f_F}{c} \sum_L \mathcal{T}_{Llm}^B \mathcal{E}_{Lm}^{\text{in}} \\ \mathcal{E}_{lm}^F &= f_F c \sum_L \mathcal{T}_{Llm}^E \mathcal{B}_{Lm}^{\text{in}}\end{aligned}\tag{42}$$

Note that the azimuthal index m doesn't change due to azimuthal symmetry.

The electric field inside the sphere is given by $\mathbf{E} = \mathbf{E}_{\text{sp}} + \mathbf{E}_F$, where \mathbf{E}_{sp} was calculated in the previous subsection and $\mathbf{E}_F \propto f_F$ is the linear correction due to the Faraday effect, to be calculated. The displacement vector is given by

$$\mathbf{D} = \epsilon_0 (\epsilon_r \mathbf{E} + i f_F \mathbf{M}_s \mathbf{z} \times \mathbf{E}).\tag{43}$$

For simplifying this further, we need the following identities

$$\mathbf{z} \times \mathbf{Y}_l^m = -\frac{im}{l(l+1)} \mathbf{Y}_l^m + g_l^m \mathbf{Z}_{l-1}^m + g_{l+1}^m \mathbf{Z}_{l+1}^m - ig_l^m \sqrt{\frac{l}{l-1}} \mathbf{X}_{l-1}^m + ig_{l+1}^m \sqrt{\frac{l+1}{l+2}} \mathbf{X}_{l+1}^m \quad (44)$$

$$\mathbf{z} \times \mathbf{X}_l^m = -\frac{m}{\sqrt{l(l+1)}} \mathbf{Z}_l^m + ig_l^m \sqrt{\frac{l}{l+1}} \mathbf{Y}_{l-1}^m - ig_{l+1}^m \sqrt{\frac{l+1}{l}} \mathbf{Y}_{l+1}^m \quad (45)$$

$$\mathbf{z} \times \mathbf{Z}_l^m = -\frac{im}{l(l+1)} \mathbf{Z}_l^m - \frac{m}{\sqrt{l(l+1)}} \mathbf{X}_l^m - g_l^m \mathbf{Y}_{l-1}^m - g_{l+1}^m \mathbf{Y}_{l+1}^m. \quad (46)$$

Here,

$$g_l^m = \sqrt{\frac{l^2 - 1}{l^2} \frac{l^2 - m^2}{4l^2 - 1}}. \quad (47)$$

These identities can be found using the known recursion relations of scalar spherical harmonics.

TE-input: Consider first a purely TE mode with angular momentum numbers LM , i.e. $\mathcal{B}_{lm}^{\text{in}} = 0$ and $\mathcal{E}_{lm}^{\text{in}} = \mathcal{E} \delta_{lL} \delta_{mM}$. For this case, we can write the VSH components of the displacement vector up to first order in f_F as

$$D_{LM}^Y \approx \epsilon_s \chi_L^E E_0 S_L(kr) \left[1 + \frac{if_F M_s}{L(L+1)} \right] + \epsilon_0 \epsilon_r E_{F,LM}^Y \quad (48)$$

$$D_{L-1,M}^X \approx -\sqrt{\frac{L}{L-1}} \epsilon_0 \epsilon_r \mathcal{I}_- S_L(kr) + \epsilon_0 \epsilon_r E_{F,L-1,M}^X \quad (49)$$

$$D_{L-1,M}^Z \approx -i \epsilon_0 \epsilon_r \mathcal{I}_- S_L(kr) + \epsilon_0 \epsilon_r E_{F,L-1,M}^Z \quad (50)$$

$$D_{L+1,M}^X \approx \sqrt{\frac{L+1}{L+2}} \epsilon_0 \epsilon_r \mathcal{I}_+ S_L(kr) + \epsilon_0 \epsilon_r E_{F,L+1,M}^X \quad (51)$$

$$D_{L+1,M}^Z \approx -i \epsilon_0 \epsilon_r \mathcal{I}_+ S_L(kr) + \epsilon_0 \epsilon_r E_{F,L+1,M}^Z, \quad (52)$$

where $\mathcal{I}_+ = g_{L+1}^M f_F M_s \chi_L^E \mathcal{E}$, and $\mathcal{I}_- = g_L^M f_F M_s \chi_L^E \mathcal{E}$. All the other coefficients are higher order in f_F . The corrections to D^Y cause a small renormalization of the Mie frequency and can be ignored.

We insert the above into the last three Maxwell's equations, Eqs. 32, and eliminate E_F^X and E_F^Z to get an equation for B_F^Y ,

$$\frac{d^2 B_{F,L\pm 1,M}^Y(r)}{k^2 dr^2} + \left(1 - \frac{(L \pm 1 + 1)(L \pm 1)}{k^2 r^2} \right) B_{F,L\pm 1,M}^Y(r) = \pm \frac{n \mathcal{I}_\pm}{c} S_{L\pm 1}(kr), \quad (53)$$

where we used the recursion relations for Riccati-Bessel functions

$$S_{l-1}(x) = S_l'(x) + \frac{l S_l(x)}{x} \quad (54)$$

$$S_{l+1}(x) = -S_l'(x) + \frac{(l+1) S_l(x)}{x}. \quad (55)$$

The general solution of this differential equation is

$$b_{L\pm 1}^Y(r) = \pm \frac{n \mathcal{I}_\pm}{c} [p_{L\pm 1}(kr) + \alpha_\pm S_{L\pm 1}(kr)], \quad (56)$$

where α_\pm are unknown constants and $p_l(x)$ is any solution satisfying

$$\frac{d^2 p_l}{dx^2} + \left(1 - \frac{l(l+1)}{x^2} \right) p_l = S_l(x) \quad (57)$$

and $p_l(0) = 0$. While it is possible to write an explicit formula for p_l , below we need only the Wronskian $W_l = p_l' S_l - p_l S_l'$ which satisfies

$$W_l'(x) = S_l^2(x) \Rightarrow W_l(x) = \frac{x}{2} [S_l^2(x) - S_{l+1}(x)S_{l-1}(x)], \quad (58)$$

where $p_l(0) = S_l(0) = 0$ is used.

So far, we found that the electromagnetic fields inside the sphere have a large component in $\{LM, TE\}$ and small Faraday scattered components in $\{L \pm 1, M, TM\}$. Via the boundary conditions, this will also hold outside the sphere, so we can write the scattered light as $\mathcal{E}_{lm} = r_L^E E_0 \delta_{lL} \delta_{mM}$ and

$$c \mathcal{B}_{lm}^F = f_F \mathcal{E} \left(P_{LM}^B \delta_{l(L+1)} \delta_{mM} + M_{LM}^B \delta_{l(L-1)} \delta_{mM} \right). \quad (59)$$

We can find these coefficients by the boundary conditions that turn out to be

$$p_{L\pm 1}(kR) + \alpha_{\pm} S_{L\pm 1}(kR) = \frac{\pm c \mathcal{B}_{L\pm 1, M}^F}{n \bar{I}_{\pm}} \xi_{L\pm 1}(k_0 R) \quad (60)$$

$$p'_{L\pm 1}(kR) + \alpha_{\pm} S'_{L\pm 1}(kR) \pm S_L(kR) = \frac{\pm c \mathcal{B}_{L\pm 1, M}^F}{\bar{I}_{\pm}} \xi'_{L\pm 1}(k_0 R). \quad (61)$$

These give

$$P_{lm}^B = -i \chi_l^E \chi_{l+1}^B g_{l+1}^m [W_{l+1}(kR) + S_l(kR)S_{l+1}(kR)] \quad (62)$$

$$M_{lm}^B = i \chi_l^E \chi_{l-1}^B g_l^m [W_{l-1}(kR) - S_l(kR)S_{l-1}(kR)] \quad (63)$$

As the calculations for the TM input are analogous, we simply write down the final result here. We define similar coefficients as above,

$$P_{lm}^E = -i \chi_l^B \chi_{l+1}^E g_{l+1}^m W_{l+1}(kR) \quad (64)$$

$$M_{lm}^E = i \chi_l^B \chi_{l-1}^E g_{l-1}^m W_{l-1}(kR). \quad (65)$$

Then, the scattering coefficients in the notation of Eqs. (42) are

$$\mathcal{T}_{Llm}^{\sigma} = P_{LM}^{\sigma} \delta_{l(L+1)} \delta_{mM} + M_{LM}^{\sigma} \delta_{l(L-1)} \delta_{mM} \quad (66)$$

For a plane wave, $E_0 e^{ik_0 z} \hat{\mathbf{x}}$, we have the input [60]

$$\mathcal{E}_{lm}^{\text{in}} = E_0 \sqrt{\pi(2l+1)} i^l (\delta_{m,1} + \delta_{m,-1}) \quad (67)$$

$$\mathcal{B}_{lm}^{\text{in}} = \frac{\mathcal{E}}{c} \sqrt{\pi(2l+1)} i^{l+1} (\delta_{m,1} - \delta_{m,-1}) \quad (68)$$

Then, the expressions for Mie and the Faraday scattered light, as written in the main text, directly follow.

B. Effective permittivity tensor of magnetic materials

For capturing the Faraday effect mathematically we derive the modified effective permittivity tensor. We can always expand the displacement vector as

$$\mathbf{D} = f_E \mathbf{E} + f_M \mathbf{M} + f_{\times} \mathbf{M} \times \mathbf{E}, \quad (69)$$

where f are functions of \mathbf{E} and \mathbf{M} . As the system is rotationally symmetric, all of f should be a function of only $|\mathbf{E}|^2$ and $\mathbf{E} \cdot \mathbf{M}$ as $|\mathbf{M}|^2$ is a constant. Assuming that there are no non-linear

optical processes, which are weak in typical materials, we need to keep only the terms that are linear in \mathbf{E} . Then, the most general form is

$$\mathbf{D} = \varepsilon_0 (\varepsilon_r \mathbf{E} + f_C \mathbf{M} \cdot \mathbf{E} \mathbf{M} + i f_F \mathbf{M} \times \mathbf{E}), \quad (70)$$

with constants $\{\varepsilon_r, f_C, f_F\}$. As the permittivity should be Hermitian, all of these constants are real.

For simplicity, we ignore the Cotton-Mouton effect ($\propto f_C$). Then, we get

$$\varepsilon_{ik}(\mathbf{M}) = \varepsilon_0 \left(\varepsilon_r \delta_{ik} - i f_F \sum_j \varepsilon_{ikj} M_j \right). \quad (71)$$

For including also dispersive magnetic materials the relative permittivity and the Faraday constant need to be made frequency dependent by using appropriate models for $\varepsilon_r(\omega)$ and $f_F(\omega)$ (see Eq. (26) in the main text).

C. Extension of the FDTD method to dispersive magnetic materials

Below we provide additional derivations used for extending the FDTD method to dispersive magnetic dielectrics.

C.1. Fourier transforms

For transforming the optical response in the frequency domain into the time domain using a Fourier transformation, the following substitutions need to be made

$$\begin{aligned} -i\omega &\rightarrow \partial_t, & -\omega^2 &\rightarrow \partial_t^2, \\ i\omega^3 &\rightarrow \partial_t^3, & \omega^4 &\rightarrow \partial_t^4. \end{aligned} \quad (72)$$

C.2. Update equations for the polarization vector

For deriving the update equation for the polarization vector we need to discretize Eq. (28) in the main text using central differencing. By centering the central differences at time step $n - 1$, the update equations for the polarization are

$$\begin{aligned} \left(\frac{1}{\Delta t^4} + \frac{\eta}{\Delta t^3} \right) \mathbf{P}^{n+1} &= \left(\frac{4}{\Delta t^4} + \frac{2\eta}{\Delta t^3} - \frac{2\omega_0^2 + \eta^2}{\Delta t^2} - \frac{\omega_0^2 \eta}{\Delta t} \right) \mathbf{P}^n + \left(-\omega_0^4 - \frac{6}{\Delta t^4} + 2 \frac{2\omega_0^2 + \eta^2}{\Delta t^2} \right) \mathbf{P}^{n-1} \\ &+ \left(\frac{4}{\Delta t^4} - \frac{2\eta}{\Delta t^3} - \frac{2\omega_0^2 + \eta}{\Delta t^2} \frac{\omega_0^2 \eta}{\Delta t} \right) \mathbf{P}^{n-2} + \left(-\frac{1}{\Delta t^4} + \frac{\eta}{\Delta t^3} \right) \mathbf{P}^{n-3} \\ &+ \omega_0^2 \varepsilon_0 (\varepsilon - 1) \left[\left(\frac{1}{\Delta t^2} + \frac{\eta}{2\Delta t} \right) \mathbf{E}^n + \left(\omega_0^2 - \frac{2}{\Delta t^2} \right) \mathbf{E}_{n-1} \right. \\ &\left. + \left(\frac{1}{\Delta t^2} - \frac{\eta}{2\Delta t} \right) \mathbf{E}^{n-1} \right] - \frac{\varepsilon_0 A_3 \omega_0}{2\Delta t} \mathbf{M} \times (\mathbf{E}^n - \mathbf{E}^{n-2}) \end{aligned} \quad (73)$$

which then include the magnetic model into the update equations via the electric field

$$\mathbf{E}^{n+1} = \mathbf{E}^n + \frac{\Delta t}{\varepsilon_0} \nabla \times \mathbf{H}^{n+1/2} - \frac{1}{\varepsilon_0} (\mathbf{P}^{n+1} - \mathbf{P}^n). \quad (74)$$

Thus, for any given time step, we need to store \mathbf{E}^{n+1} , \mathbf{E}^n , \mathbf{E}^{n-1} , \mathbf{E}^{n-2} , \mathbf{P}^{n+1} , \mathbf{P}^n , \mathbf{P}^{n-1} , \mathbf{P}^{n-2} , and \mathbf{P}^{n-3} .